nature materials

SUPPLEMENTARY INFORMATION
https://doi.org/10.1038/s41563-019-0354-z

In the format provided by the authors and unedited.

Gap suppression at a Lifshitz transition in a multi-condensate superconductor

G. Singh[1,2], A. Jouan[1,2], G. Herranz[3], M. Scigaj[3], F. Sánchez[3], L. Benfatto[4,5], S. Caprara[4,5], M. Grilli[4,5], G. Saiz[1,2], F. Couëdo[1,2], C. Feuillet-Palma[1,2], J. Lesueur[1,2] and N. Bergeal[1,2*]

[1]Laboratoire de Physique et d'Etude des Matériaux, ESPCI Paris, PSL Research University, CNRS, Paris, France. [2]Université Pierre and Marie Curie, Sorbonne-Université, Paris, France. [3]Institut de Ciéncia de Materials de Barcelona (ICMAB-CSIC), Campus de la UAB, Bellaterra, Catalonia, Spain. [4]Institute for Complex Systems (ISC-CNR), UOS Sapienza, Roma, Italy. [5]Dipartimento di Fisica Università di Roma 'La Sapienza', Roma, Italy.
*e-mail: nicolas.bergeal@espci.fr

Gap suppression at a Lifshitz transition in a multi-condensate superconductor : Supplementary Information

G. Singh[1,2], A. Jouan[1,2], G. Herranz[3], M. Scigaj[3], F. Sánchez[3], L. Benfatto[4,5], S. Caprara[5,4], M. Grilli[5,4], G. Saiz[1,2], F. Couedo[1,2], C. Feuillet-Palma[1,2], J. Lesueur[1,2], N. Bergeal[1,2*]

[1] *Laboratoire de Physique et d'Etude des Matériaux, ESPCI Paris, PSL Research University, CNRS, 10 Rue Vauquelin - 75005 Paris, France.*

[2] *Université Pierre and Marie Curie, Sorbonne-Universités, 75005 Paris, France.*

[3] *Institut de Ciéncia de Materials de Barcelona (ICMAB-CSIC), Campus de la UAB, 08193 Bellaterra, Catalonia, Spain.*

[4] *Institute for Complex Systems (ISC-CNR), UOS Sapienza, Piazzale A. Moro 5, 00185 Roma, Italy*

[5] *Dipartimento di Fisica Università di Roma "La Sapienza", Piazzale A. Moro 5, I-00185 Roma, Italy.*

Supplementary Note 1 : Two-band superfluid stiffness analysis

The temperature dependence of the normalised superfluid stiffness in the OD regime was analysed using the model developed in reference [2]. We consider two superconducting bands with density of states $N_{1,2}$ and interband coupling constants $\lambda_{11(22)}$. In addition, we add a small interband coupling between the two bands characterised by the constants $\lambda_{12(21)}$. In this BCS approach, the superconducting T_c is determined by the following equation :

$$1.76 k_B T_c = 2E_D \exp(-\frac{1}{\tilde{\lambda}}) \tag{1}$$

where E_D=400K is the Debye energy [1] and $\tilde{\lambda}$ the effective coupling constant given by

$$\tilde{\lambda} = \frac{2(\lambda_{11}\lambda_{22} - \lambda_{12}\lambda_{21})}{\lambda_{11} + \lambda_{22} - \sqrt{(\lambda_{11} - \lambda_{22})^2 + 4\lambda_{12}\lambda_{21}}} \tag{2}$$

For the interband coupling terms we assume that $\frac{\lambda_{12}}{n_2} = \frac{\lambda_{21}}{n_1}$, where $n_1 = \frac{N_1}{N_1+N_2} \simeq 0.6$ and $n_2 = \frac{N_2}{N_1+N_2} \simeq 0.4$ are the density of states weight in each band, which are determined from the average in-plane masses (see Supplementary Note 2). We introduce the dimensionless gap energies

$$\delta_\nu = \frac{\Delta_\nu}{2\pi k_B T} \tag{3}$$

which is given by solving self-consistently the two following equations

$$\delta_\nu = \sum_{\mu=1,2} \lambda_{\nu\mu}\delta_\mu \Big(\frac{1}{\tilde{\lambda}} + \ln\frac{T_c}{T} - A_\mu\Big) \tag{4}$$

$$A_\mu = \sum_{n=0}^{\infty} \Big(\frac{1}{n+1/2} - \frac{1}{\sqrt{\delta_\mu^2 + (n+1/2)^2}}\Big) \tag{5}$$

For each band the temperature dependence of the associated normalized stiffness is derived from the dimensionless gap energy δ_ν

$$j_{s\nu} = \delta_\nu^2 \sum_{n=0}^{\infty} [\delta_\nu^2 + (n + 1/2)^2]^{-3/2} \tag{6}$$

The total normalized stiffness is the sum of the contributions of each band

$$j_s = \gamma j_{s1} + (1 - \gamma) j_{s2} \tag{7}$$

where the γ coefficient accounts for the weight of each band in the superfluid condensate. Data shown in Figure 4 of the main text has been fitted using the relations (6) and (7). In the case of a single-gap, corresponding to the underdoped regime, the energy gap at T=0 K is simply given by the BCS relation $\Delta = 1.76 k_B T_c$ (Eq.1). In the overdoped regime, the gap-to-T_c ratio remains close to 1.76 for the largest gap (Δ_2) because of the low interband coupling. Figure 5c of the article shows the evolution of the γ coefficient with the gate voltage.

The model of Kogan *et al.* is derived in the clean limit. However, while disorder affects the absolute values of the superfluid stiffness, its temperature dependence remains only marginally affected. Indeed, the temperature evolution of J_s is crucially controlled by $\Delta(T)$. In the single-band case, J_s decreases exponentially in $\Delta(T)/T$ at low temperature and as $\Delta^2(T) \sim (1 - T/T_c)$ near T_c. These two limiting behaviors are observed experimentally and reproduced theoretically both in the clean and dirty limit, since they reflect a rather universal behavior of the superconducting system (the thermal excitation of quasiparticles across the gap at low temperature and the vanishing of the superconducting order parameter near T_c). Note that in this pure BCS approach, the effect of fluctuations has not been included.

In Supplementary Figure 7 we show the doping dependence of the dimensionless coupling constant extracted from the analysis of the superfluid stiffness. As explained in the method section, $\tilde{\lambda}$ is the effective coupling determining the T_c. In the single-band case, it coincides with λ_{11}, while for the multiband regime it is given by Eq. (2). As mentioned in the main text, the analysis of the temperature dependence of the superfluid density relies mainly on the relative band filling and on the gap values, so it is a robust finding rather insensitive to the presence of disorder. On the other hand, $\Delta_\nu(T)$ must be derived using a specific model for the superconducting state. To simplify the analysis, we relied on the Eq.s (3)-(5), where the gap are computed for a multiband model in the absence of disorder. In this case, the only way to obtain a decrease of the gap values at $T = 0$ is to reduce the coupling constants, as shown in Supplementary Figure 6. However, a similar result could be possibly obtained by using constant superconducting couplings and introducing the effect of disorder. Indeed, as recently discussed in Ref. [4], in the presence of disorder a $s_\pm$ superconducting state is strongly affected by the onset of occupancy of the secondary band. Indeed, interband impurity scattering is pair breaking in a $s_\pm$ superconductor, leading to a gradual suppression of both the critical temperature and of the superconducting gap across the Lifshitz transition. A quantitative analysis of this effect requires however a detailed analysis of a dirty multiband model that is well beyond the scope of the present work.

Supplementary Note 2 : Interfacial band structure simulation

The filling and the confinement of each t_{2g} band are determined by solving self-consistently the Schrödinger and the Poisson equations as described in the supplementary material of reference [5]. The hopping terms in Fig 1a. were taken to be t_1=-320meV and t_2=-16meV, which correspond to the masses $m_{001}^{xz,yz} = -\frac{\hbar^2}{2a^2 t_1} \simeq 0.7\mathrm{m}_0$ for the $d_{xz/yz}$ orbitals and $m_{001}^{xy} = -\frac{\hbar^2}{2a^2 t_2} \simeq 14\mathrm{m}_0$ for the d_{xy} orbitals along the (001) direction of the conventional (001)-oriented interfaces. In the (110)-oriented interfaces, the masses along the confinement direction (i. e. the (110) direction) are $m_{110}^{xz,yz} = -\frac{\hbar^2}{2a^2(t_1+t_2)} \simeq 0.65\mathrm{m}_0$ and $m_{110}^{xy} = -\frac{\hbar^2}{4a^2 t_1} \simeq 0.35\mathrm{m}_0$ [6]. The density of states can be determined from the in-plane masses in the (1-10) and (001) directions. For the d_{xy} orbital, $m_{001}^{xy} = -\frac{\hbar^2}{2a^2 t_2} \simeq 14\mathrm{m}_0$ and $m_{1-10}^{xy} = -\frac{\hbar^2}{2a^2 t_1} \simeq 0.7\mathrm{m}_0$, corresponding to an average in-plane mass $m_{\parallel}^{xy} = \sqrt{m_{001}^{xy} m_{1-10}^{xy}} \simeq 3.1\mathrm{m}_0$ [6]. For the $d_{xz,yz}$ orbitals, $m_{001}^{xz,yz} = -\frac{\hbar^2}{2a^2 t_1} \simeq 0.7\mathrm{m}_0$ and $m_{1-10}^{xz,yz} = -\frac{\hbar^2}{2a^2\left(\frac{2t_1 t_2}{t_1+t_2}\right)} \simeq 7.3\mathrm{m}_0$, corresponding to an average in-plane mass $m_{\parallel}^{xz,yz} = \sqrt{m_{001}^{xz,yz} m_{1-10}^{xz,yz}} \simeq 2.3\mathrm{m}_0$ [6].

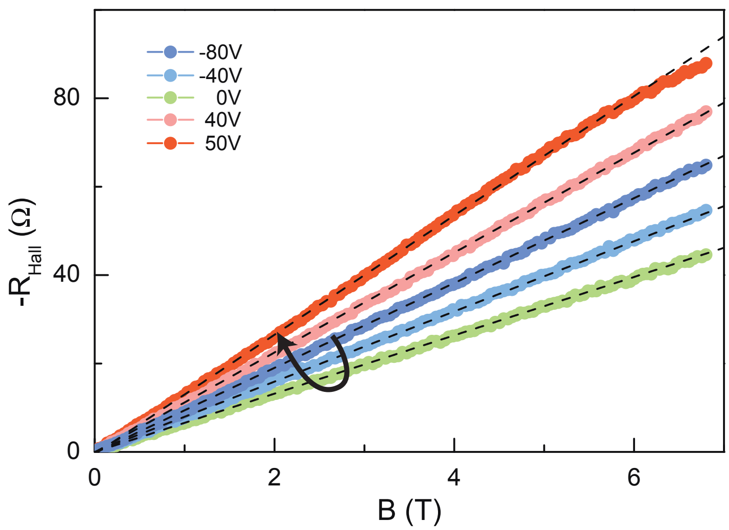

Supplementary Figure 1: **Linear and non-linear Hall effect.** Hall resistance as a function of magnetic field applied perpendicular to the interface for different gate values. The Hall effect is linear in magnetic field, corresponding to one-band transport for $V_{\mathrm{G}} < V_{\mathrm{G}}^{\mathrm{opt}} \simeq$-10 V and becomes non-linear for higher gate voltages corresponding to two-band transport. However, as the non-linearity develops at high magnetic field is starts to be clearly visible only for the highest gate voltage (V_{G}=50V). A full analysis of this non-linearity would require to access very high-magnetic field as in reference [5]. Nonetheless, the single-band to two-band transition can be clearly identified by the sudden change in behaviour of the low magnetic field slope of the Hall curves (see arrow in the figure). While for $V_{\mathrm{G}} < V_{\mathrm{G}}^{\mathrm{opt}}$ the slope decreases with gate voltage as expected when carriers are added in the 2-DEG, for $V_{\mathrm{G}} > V_{\mathrm{G}}^{\mathrm{opt}}$ this slope increases with gate voltage corresponding to the drop of $n_{\mathrm{Hall}} = \frac{B}{eR_{\mathrm{H}}}$ in Fig. 1e of the article. As shown in reference [5], the total carrier density can be retrieved by considering the charging curve of the gate capacitor (n_{2DEG} in Fig1.e) or by performing Hall effect at much higher magnetic field.

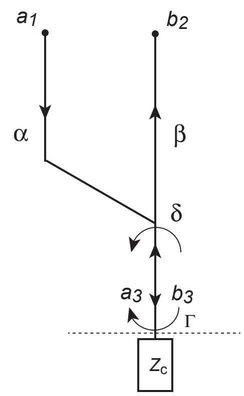

Supplementary Figure 2: **Modeling of the microwave set-up using the scattering matrix formalism**. a_i and b_i denote the complex amplitude of the incoming and outgoing waves at point i. We assume that the VNA connected to port 1 and 2 is perfectly matched to the 50Ω coaxial cables of the set-up, which implies that no signal is reflected at port 1 and port 2. $\alpha(\omega)$, $\beta(\omega)$, $\gamma(\omega)$ and $\delta(\omega)$ are complex coefficients representing the transmission and reflection coefficients in the various points of the circuit, which satisfy the relations $a_3 = \delta b_3 + \alpha a_1$ and $b_2 = \gamma a_1 + \beta b_3$. The transmission coefficient between port 1 and port 2, $S_{21}(\omega) = b_2(\omega)/a_1(\omega)$, is related to the reflection coefficient of the sample circuit, $\Gamma(\omega) = b_3(\omega)/a_3(\omega)$, through $S_{21} = \gamma + \frac{\alpha'\Gamma}{1-\delta\Gamma}$ where $\alpha' = \alpha\beta$. The error complex coefficients can be determined using three known values of Γ which are obtained by imposing three different impedances Z_c (see reference [7] for details on the calibration procedure).

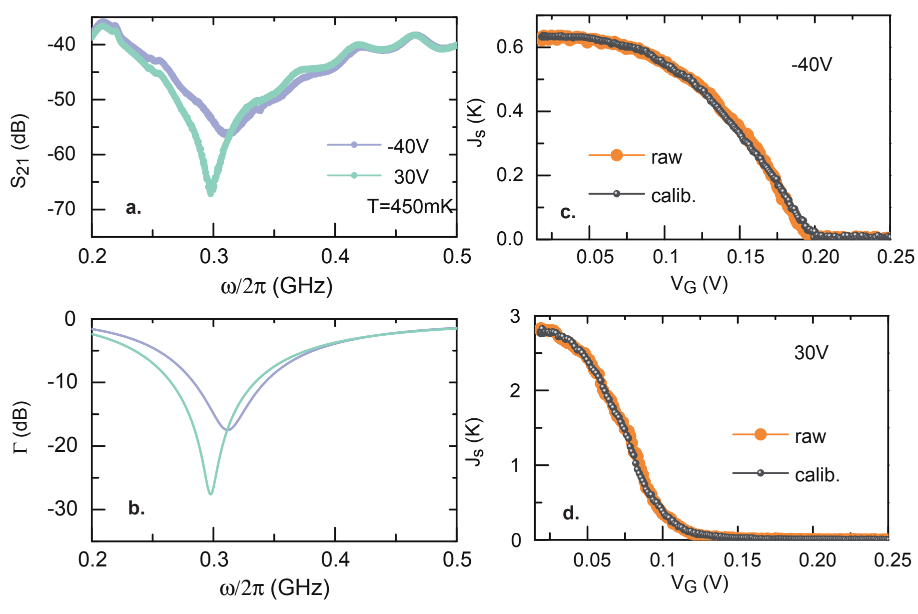

Supplementary Figure 3: **Comparison between raw data and calibrated data.**. a) Magnitude of the transmission coefficient S_{21} measured at T = 450 mK for V_G= -40 V and for V_G= 30 V. The resonance frequency is clearly visible on both curves. b) Reflection coefficient Γ of the sample circuit extracted from S_{21} after calibration (see Methods section and Supplementary Figure 2. c)$J_s(T)$ extracted from raw data and calibrated data for V_G= -40 V. d) $J_s(T)$ extracted from raw data and calibrated data for V_G= 30 V.

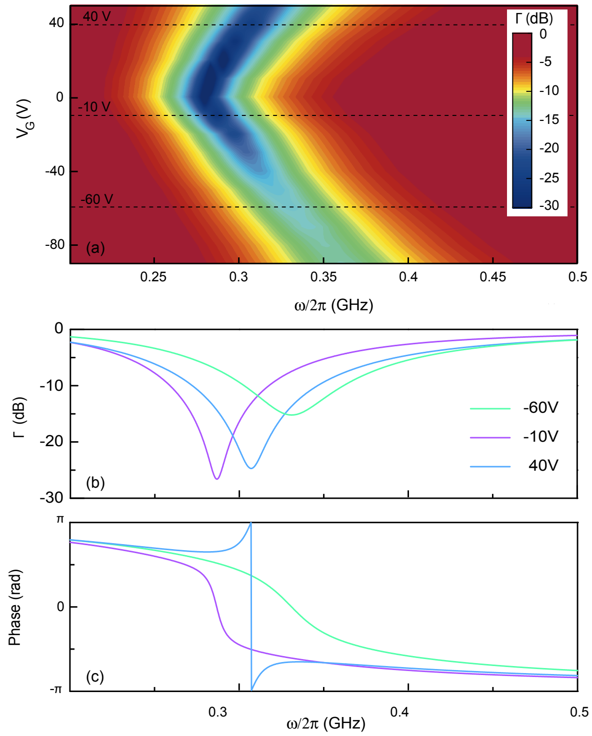

Supplementary Figure 4: (a) Magnitude of Γ in dB (color scale) as a function of ω and $V_{\rm G}$ measured at T=450 mK. C_{sto} takes a maximum value of 36 pF for $V_{\rm G} = 0$ V. Magnitude (panel b) and phase (panel c) of Γ for three gate voltages $V_{\rm G}$ =-60V (underdoped), $V_{\rm G}$=-10V (optimally doped) and $V_{\rm G}$=40V (overdoped), corresponding to dashed lines in panel a.

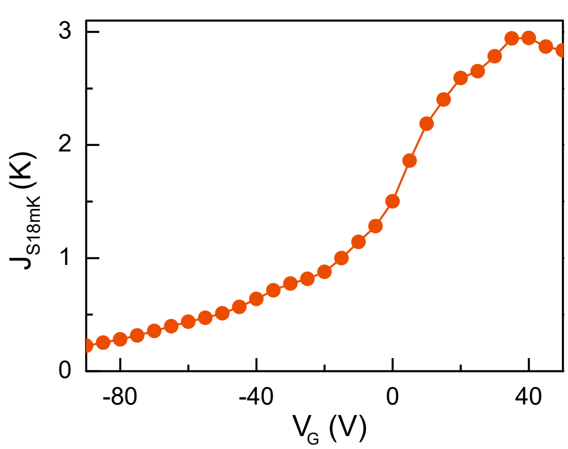

Supplementary Figure 5: Gate dependence of J_s extracted from $\Gamma(\omega)$ at the lowest temperature T≃18mK.

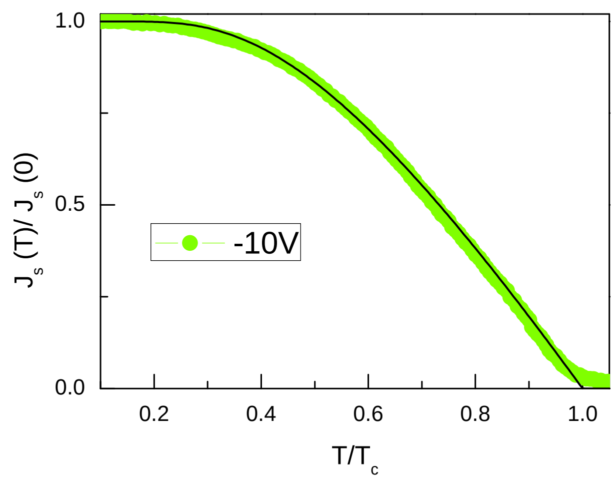

Supplementary Figure 6: Temperature dependence of normalised superfluid stiffness $j_s(T)$ at the optimal doping point $V_{\rm G}$=-10V fitted by a single band BCS model.

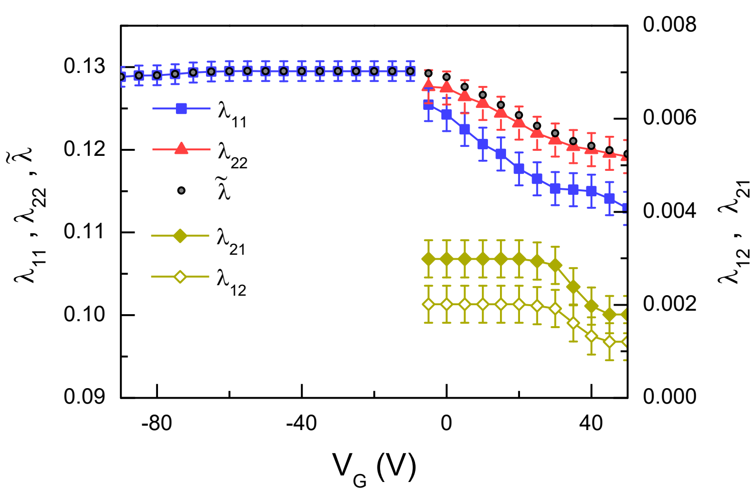

Supplementary Figure 7: Gate dependence of the coupling constants in the phase diagram. The main source of pairing is the positive intraband coupling $\lambda_{11(22)}$ with a small interband coupling $\lambda_{12(21)}$ which can be either positive (attractive) or negative (repulsive). The values of the coupling constants are found to be comparable to the rare values reported in the literature for bulk $SrTiO_3$ [3]

.

[1] Maniv, E. et al. Strong correlations elucidate the electronic structure and phase diagram of $LaAlO_3/SrTiO_3$ interface. *Nat. Commun.* **6**, 8239 (2015).

[2] Kogan, V. G., Martin, C., Prozorov, R. Superfluid density and specific heat within a self-consistent scheme for a two-band superconductor. *Phys. Rev. B* **80**, 014507 (2009).

[3] Fernandes, R. M., Haraldsen, J. T., Wölfle, P. and Balatsky, A. V. Two-band superconductivity in doped $SrTiO_3$ films and interfaces. *Phys. Rev. B* **87**, 014510 (2013).

[4] Trevisan, T. V., Schütt, M., Fernandes, R. M. Unconventional multi-band superconductivity in bulk $SrTiO_3$ and $LaAlO_3/SrTiO_3$ interfaces. *Phys. Rev. Lett.* **121**, 127002 (2018).

[5] Biscaras, J., Bergeal, N., Hurand, S., Grossetete, C., Rastogi, A. Budhani, R. C., LeBoeuf, D., Proust, C. and Lesueur, J. Two-dimensional superconductivity induced by high-mobility carrier doping in $LaTiO_3/SrTiO_3$ heterostructures. *Phys. Rev. Lett.* **108**, 247004 (2012).

[6] Wang, Z. *et al.* Anisotropic two-dimensional electron gas at $SrTiO_3$ (110). *Proc. Natl. Acad. Sci.* **111**, 3933-7 (2014).

[7] Singh, G. *et al.* Competition between electron pairing and phase coherence in superconducting interfaces. Nat. Commun. **9**, 407 (2018).